Numerical determination of iron dust laminar flame speeds with the counter-flow twin-flame technique

Combustion and Flame 266 (2024) 113524

Contents lists available at ScienceDirect

Combustion and Flame

journal homepage: www.sciencedirect.com/journal/combustion-and-flame

Numerical determination of iron dust laminar flame speeds with the counter-flow twin-flame technique

C.E.A.G van Gool *, T. Hazenberg, J.A. van Oijen, L.P.H. de Goey

Department of Mechanical Engineering, Eindhoven University of Technology, P.O. Box 513, NL-5600 MB, Eindhoven, The Netherlands

ARTICLE INFO

Keywords:
Iron
Dispersed-phase flame
Counter-flow
Particle flow strain
Burning velocity

ABSTRACT

Iron dust counter-flow flames have been studied with the low-Mach-number combustion approximation. The model considers full coupling between the two phases, including particle/droplet drag. The dispersed phase flow strain relations are derived in the Stokes regime (Reynolds number much smaller than unity). The importance of solving a particle flow strain model is demonstrated by comparing three different cases: a free unstrained flame, a counter-flow flame where slip effects are neglected and a counter-flow flame where slip effects are included. All three cases show preferential diffusion effects, due to the lack of diffusion of iron in the fuel mixture, e.g. $D_{\mathrm{Fe},m} = 0$. The preferential diffusion effect causes a peak in the fuel equivalence ratio in the preheat zone. On the burned side, the combined effect of strain and preferential diffusion shows a decrease in fuel equivalence ratio. Inertia effects, which are only at play in the counter-flow case with slip, counteract this effect and result in an increase of the fuel equivalence ratio on the burned side. A laminar flame speed analysis is performed and a recommendation is given on how to experimentally determine the flame speed in a counter-flow set-up.

Novelty & Significance

We introduce a novel model to include particle flow strain in a dispersed counter-flow set-up. For the first time, the impact of particle flow strain on the flame structure of iron dust is studied with a one-dimensional (1D) model. Two major effects that modify the flame structure and burning velocity are identified: preferential diffusion and inertia of the particles. Preferential diffusion effects are found to be always present in (iron) dust flames. Inertia effects play a role in the counter-flow case with slip. Due to the inertia of the particles, the particle flow strain is lower than the gas flow strain. As a consequence, higher particle concentrations are reached compared to the other cases. Furthermore, it is shown that each particle size experiences a different particle flow strain rate, which is important when doing experiments as it implies that the PSD at the flame front will be different than at the inlet.

1. Introduction

Recently, a lot of research is performed to investigate the possibility of using iron powder as a zero-carbon fuel [1–7]. In closed-loop metal-fuel cycles, iron powder can be oxidized when power and/or heat is required. The formed oxides can be reduced at other places and other times using hydrogen, obtained via renewable energy sources. For the development of practical iron fuel-burning set-ups a thorough understanding on iron combustion characteristics is required. A key parameter for fundamental and practical purposes is the laminar burning velocity, s_{L}.

For gaseous flames it is well known that laminar flame speeds can be substantially modified by stretch effects such as flow non-uniformity, flame curvature, and flame/flow unsteadiness [8–13]. These effects must be taken into consideration for an accurate prediction of the laminar flame speed. For that reason, Wu and Law [11] proposed the development of the counter-flow twin-flame technique for the determination of s_{L}. The first analytical studies of stretched flames were based on models with reduced complexity, with e.g. a single Lewis number, a single reversible reaction, and a flame sheet. Later on, the flame stretch theory was extended to more general flames, with finite flame front thickness [13,14]. For iron flames, stretch effects are also at play. Moreover, additional complexity is expected when the condensed phase comprises a substantial fraction of the total momentum of the flow, but not having the same velocity as the surrounding gas.

When iron particles are exposed to a strained gas flow, like in the case of a counter-flow, the gas is continuously accelerating tangential to

* Corresponding author.
E-mail address: c.e.a.g.v.gool@tue.nl (C.E.A.G van Gool).

https://doi.org/10.1016/j.combustflame.2024.113524
Received 7 October 2023; Received in revised form 16 May 2024; Accepted 17 May 2024
Available online 29 May 2024

the flame surface and so is the dispersed phase. The dispersed phase is dragged by the gas and therefore moves slower. A similar phenomenon is observed for coal particles flow and liquid droplet flow strained by gas flow [15,16]. The lagging of the particle flow with respect to the gas flow can also be observed in the work of Wen et al. [17], where iron dust flames have been studied with a 3D counter-flow model. In their work, very small particles are used (a mean diameter of $d_{50} = 1.4\mu m$), which means that a high particle concentration is required, resulting in high computational costs. In the work of Zhang et al. [18] aluminum dust counter-flow flames are investigated, also in a 3D framework. Their work utilizes a 2-staged combustion process, consisting of a pre-heating/ heterogeneous surface reaction stage and a quasi-steady combustion stage, where the heterogeneous surface reactions cannot occur simultaneously with the combustion stage.

The goal of this paper is to quantify the effects of drag/strain and preferential diffusion of a general aerosol flame, with a focus on iron/air aerosols. The particle model used in this work, is based on the model of Hazenberg and van Oijen [5]. A new model is derived to describe the particle flow strain as function of the gas flow strain in the Stokes regime (Reynolds number much smaller than unity). With this model, the impact of strain on the burning velocity is investigated in a quasi-1D counterflow dispersed twin-flame configuration. Furthermore, extrapolation to zero strain (see e.g., [11]) is performed to obtain strain-free laminar burning velocities. The particle strain model, does not limit itself to iron particles, it is also valid for other dispersed fuels that burn heterogeneously.

The derivation of a detailed and reduced one-dimensional (1D) particle flow strain model is presented in Section 2. Then, in the first part of Section 3 the preferential diffusion effects in a dispersed flame are discussed. In the second part, the influence of particle strain on the flame structures is investigated. Next, particle flow strain effects for different particle sizes are analyzed. In the last subsection of Section 3, two methods to measure the burning velocity are discussed. Finally, a discussion and the main conclusions are given in Section 4.

2. Model description

The case of planar opposed flow nozzles, at a distance L from each other, is considered. Compositions and velocities, at temperature T_u =300 K, are assumed uniform and equal at the nozzle exits. Therefore, the system is symmetric with respect to the stagnation plane. Under specific assumptions, which will be discussed in the remainder of this chapter, the system can be considered as quasi-1D. A schematic representation of the configuration is provided in Fig. 1. Due to symmetry at the stagnation plane, only half of the domain is simulated. The iron-air flame is modeled with an Euler–Lagrange approach, similarly as in [5,7]. In this study, we extend that framework with 1D strain equations to model the counter-flow set-up.

2.1. Particle model

The dispersed phase is modeled in a Lagrangian framework, where single particles are tracked in one-dimensional space such that the Lagrangian time-coordinate can be related to the Eulerian spatial-coordinate. The equations for mass m_p, enthalpy H_p and velocity in the x-direction, u_p, see Fig. 1 for the definition of the coordinates, for a single particle are given by:

$$\frac{\mathrm{d}m_p}{\mathrm{d}t} = Y_{O_2} A_d k_d \mathrm{Da}^*, \tag{1}$$

$$\frac{\mathrm{d}H_p}{\mathrm{d}t} = k_c A_p \left(T_g - T_p\right) + \frac{\mathrm{d}m_p}{\mathrm{d}t} h_{O_2}, \tag{2}$$

$$\frac{\mathrm{d}u_p}{\mathrm{d}t} = \frac{3}{4}\frac{C_D \rho_g}{d_p \rho_p}\left|u_g - u_p\right|\left(u_g - u_p\right), \tag{3}$$

$$\frac{\mathrm{d}x_p}{\mathrm{d}t} = u_p, \tag{4}$$

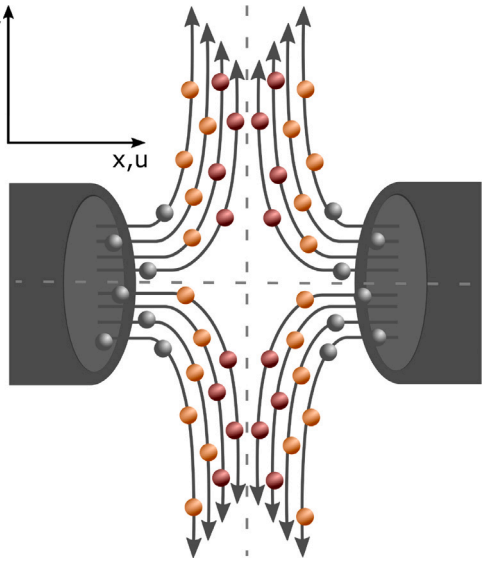

Fig. 1. Schematic representation of a 1D counter-flow flame. The particle colors indicate: gray an unburned particle, orange a partially oxidized particle, and red a fully oxidized particle. (For interpretation of the references to colour in this figure legend, the reader is referred to the web version of this article.)

where Y_{O_2} is the mole fraction of oxygen in the carrier gas, k_d the mass-transfer coefficient for a sphere and Da^* the normalized Damköler number [5]. In this work, the core-in-shell model is employed, based on a proposed combustion mode by Bergthorson et al. [2]. It is assumed that the metal-oxide shell is non-protective and reactions occur at the metal - metal-oxide interface, such that the reactive area is defined as $A_r = \left(m_{p,Fe}/m_p\right) A_p$, with $m_{p,Fe}$ the unburned mass of the particle. The diffusive surface area is equal to the particle surface area, $A_d = A_p$, with $A_p = \pi d_p^2$. The heat transfer coefficient is given by k_c, the gas and particle temperature are T_g and T_p and the mass-specific enthalpy of the consumed oxygen h_{O_2}, which is required as the enthalpy H_p consists of both the sensible and chemical part of the enthalpy. Finally, ρ_p and ρ_g are the particle and gas density, d_p is the particle diameter, x_p the particle position and C_D the drag coefficient. The drag coefficient is formulated by an empirical relation for low Reynolds number [19],

$$C_D = \frac{24}{\mathrm{Re}}\left(1 + 0.15\mathrm{Re}^{0.687}\right). \tag{5}$$

The particle Reynolds number Re is defined as,

$$\mathrm{Re} = \frac{d_p |u_g - u_p| \rho_g}{\mu_g} \tag{6}$$

with μ_g the dynamic viscosity of the carrier gas in the particle film layer.

The coupling between gas and dispersed phase is handled as in Sacomano Filho et al. [20]. Since the particles are solved in a Lagrangian framework, the time dependent variables have to be transformed to position dependent variables. Let the temporal solution of Eq. (4) be: $x_p = g(t)$, then the inverse function gives t as function of x, i.e. $t = g^{-1}(x)$. The temporal solution for the change of mass, Eq. (1), can be written as: $\frac{\mathrm{d}m_p}{\mathrm{d}t} = f_m(t)$. The other time dependent variables can be described in the same way such that the mass and enthalpy exchange between the phases, denoted as S_m and S_h, have the form:

$$S_m = f_{N_p}\left(g^{-1}(x)\right) f_m\left(g^{-1}(x)\right), \tag{7}$$

$$S_H = f_{N_p}\left(g^{-1}(x)\right) f_H\left(g^{-1}(x)\right), \tag{8}$$

with $\dot{N}_p = f_{N_p}(t)$ the number flux.

For model closure terms and further details of the particle model, we refer to the work of Hazenberg et al. [5,21]. As a first step, the

oxidation beyond FeO as presented in Gool et al. [7] is not included here.

2.2. Gas-phase modeling

The counterflow-twin flame is modeled as a steady quasi-1D strained flame, where the low-Mach number combustion-approximation is assumed [22]. The finite volume solver CHEM1D is used to solve these equations [23]. The quasi-1D conservation equations, read:

$$\frac{\partial}{\partial x}(\rho u) = S_m - \rho a_g \tag{9}$$

$$\frac{\partial}{\partial x}\left(\rho u Y_i\right) + \frac{\partial}{\partial x}\left(\rho U_i Y_i\right) = \delta_{i,k} S_m - \rho a_g Y_i \tag{10}$$

$$\frac{\partial}{\partial x}(\rho u h) + \frac{\partial q}{\partial x} = S_h - \rho a_g h \tag{11}$$

with U_i the diffusion velocity of species i. Since oxygen and nitrogen are the only species in the gas phase, and nitrogen is used to ensure conservation of mass, the i in Eq. (10) equals the index of oxygen. As there is only exchange of oxygen, the k in the Kronecker delta $\delta_{i,k}$ equals the index of oxygen. The transport of enthalpy due to mass diffusion and conduction in the gas phase is defined as

$$q = -\frac{\lambda}{c_p}\frac{\partial h}{\partial x} + \sum_{i=1}^{N_s} h_i \left(\frac{\lambda}{c_p}\frac{\partial Y_i}{\partial x} - \rho U_i Y_i\right). \tag{12}$$

Since we consider a steady planar flame of finite thickness, the flame properties are assumed to only be a function of the x-direction [12,15], i.e., $\rho(x)$, $T(x)$, $Y_i(x)$, etc. The only property which is a function of both the x- and y-direction is the y-velocity $v(x, y)$. In this work, we are only interested in the solution around $y = 0$, which is the location where measurements are performed. We assume that variations in the y-direction are small and at $y = 0$, there is no velocity in the vertical direction, meaning $v(x, 0) = 0$. Performing a first order Taylor expansion around the x-axis on the velocity in the y-direction results in

$$v(x, y) = y\frac{\partial v}{\partial y}\Big|_{y=0} = ay + \mathcal{O}\left(y^3\right), \tag{13}$$

where we notice that $a(x) = \frac{\partial v}{\partial y}$ denotes the flow strain rate in the direction tangential to the flame surface, applicable for both particles a_p and gas a_g. Similar to the work of Dixon-Lewis [12] we assume that higher order velocity terms are negligible. On top of that, even derivatives are zero anyway due to the assumption of symmetry around $y = 0$, hence the 3rd order truncation error. Since the Taylor expansion is done around $y = 0$, the strain can thus be written as $a = v/y$, which will be useful later for the derivation of the particle flow strain model in the next subsection.

The solution for the gas flow strain, a_g, is obtained through solving an additional transport equation:

$$\frac{\partial\left(\rho u a_g\right)}{\partial x} - \frac{\partial}{\partial x}\left(\mu\frac{\partial a_g}{\partial x}\right) = S_a + J - \rho a^2 \tag{14}$$

where the exchange of momentum between dispersed and gas phase has the form $S_a = f_{N_p}\left(g^{-1}(x)\right) f_a\left(g^{-1}(x)\right)$, and $J = -\frac{1}{y}\frac{\partial p}{\partial y}$ is the tangential pressure gradient. With $f_a(t)$ containing the temporal solution of the strain rate $\frac{da_p}{dt}$, see Eq. (22) in the next subsection. In Appendix A the derivation of Eq. (14) is included.

2.3. Particle strain model

In Eq. (13) we showed a general expression for the flow strain, which is valid for both the gas and the particle flow strain. For the particle flow strain, we require an expressions for v_p and y_p to obtain a linear approximation to the particle flow strain. The time derivative of the particle velocity in the y-direction can be described as,

$$\frac{dv_p}{dt} = \frac{3}{4}\frac{C_D\rho_g}{d_p\rho_p}\left|v_g - v_p\right|\left(v_g - v_p\right) \tag{15}$$

with v_g the gas velocity in the y-direction. Substituting Eqs. (5) and (6) in Eq. (15) gives,

$$\frac{dv_p}{dt} = \frac{18\mu}{d_p^2\rho_p}\left(v_g - v_p\right)\left(1 + 0.15\mathrm{Re}^{0.687}\right). \tag{16}$$

Since we estimate Re to be at most in the order of 10^{-3} in our work (small particles and small slip velocity), we assume that $\mathrm{Re} \ll 1$, which also follows from the Taylor expansion around $y = 0$, such that we can linearize Eq. (16) around $\mathrm{Re} = 0$ which results in,

$$\frac{dv_p}{dt} = \frac{18\mu_g}{d_p^2\rho_p}\left(v_g - v_p\right) = \frac{v_g - v_p}{\tau}, \quad \text{with } \tau = \frac{d_p^2\rho_p}{18\mu_g}. \tag{17}$$

Only for this linearization it is assumed that $\mathrm{Re} = 0$ and nowhere else. Substituting $v_p = \frac{dy_p}{dt}$, a second order differential equation for particle position in y-direction y_p is obtained

$$\frac{d^2y_p}{dt} + \frac{1}{\tau}\frac{dy_p}{dt} - \frac{a_g}{\tau}y_p = 0, \tag{18}$$

with $a_g = \frac{v_g}{y_p}$ the gas strain at y_p, the particle position. Notice that y_p is the only variable in Eq. (18), when assuming that τ and a_g are constant. Further assuming they are positive, the general solution of Eq. (18) becomes

$$y_p = c_1\exp\left(r_1 t\right) + c_2\exp\left(r_2 t\right), \qquad \text{with} \tag{19}$$

$$r_1 = -\frac{1}{2\tau} + \sqrt{\frac{1}{4\tau^2} + \frac{a_g}{\tau}}, \qquad r_1 > 0,$$

$$r_2 = -\frac{1}{2\tau} - \sqrt{\frac{1}{4\tau^2} + \frac{a_g}{\tau}}, \qquad r_2 < 0. \tag{20}$$

Then, by using the definition of strain and substituting the general solution for particle position and its derivative, an expression can be obtained for the particle strain for $t \to \infty$ when the strain has reached equilibrium:

$$a_{p,eq} = \frac{v_{p,eq}}{y_{p,eq}} = \frac{c_1 r_1\exp\left(r_1 t\right) + c_2 r_2\exp\left(r_2 t\right)}{c_1\exp\left(r_1 t\right) + c_2\exp\left(r_2 t\right)}\Big|_{t\to\infty} = r_1. \tag{21}$$

For $t \to \infty$, the terms with r_2 go to zero. r_2 can physically be interpreted as the adjusting rate of the particle flow field when subjected to a continuous gas flow strain. In a continuously strained flow field, the particle is not able to follow the accelerating gas due to inertia. Provided the above, we propose a reduced model:

$$\frac{da_p}{dt} = \frac{a_{p,eq} - a_p}{\tau_{a_p}}, \tag{22}$$

which is a one equation model that reaches the in Eq. (21) derived strain within timescale $\tau_{a_p} = -1/r_2$. In a counter-flow set-up, the coefficients a_g and τ are not constant. Nevertheless, the above reduced model is still used, where a_g and τ are evaluated at the particle position, i.e., $a_{p,eq}$ and τ_{a_p} are dependent on the local gas composition and flow. In Appendix B the reduced particle flow strain model in Eq. (22) is compared with the detailed solution obtained via Eq. (18), for cases in which the coefficients are not constant. We do not find significant differences between the models.

The particle flow strain acts as a sink term ($a_p \geq 0$ and $a_g > 0$ in counter-flow flames) on the particle number flux $\dot{N}_p$. This means that an additional equation for the change in particle number flux $\dot{N}_p$

$$\frac{d\dot{N}_p}{dt} = -a_p\dot{N}_p \tag{23}$$

is solved.

2.4. Boundary conditions

There are two sets of boundary conditions possible to solve the flow strain in the setup shown in Fig. 1. One can either prescribe the strain

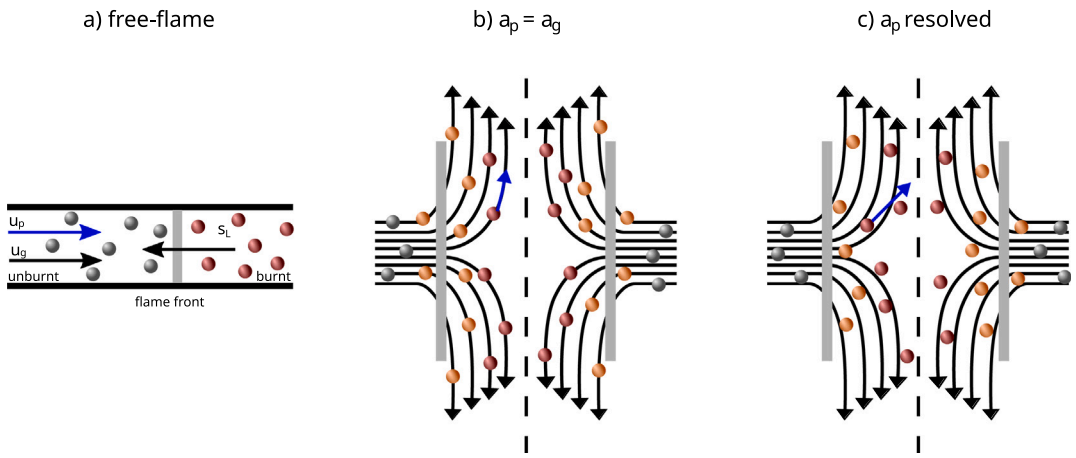

Fig. 2. Schematic representation of (a) a one-dimensional planar flame, (b) a stagnation flame with $a_p = a_g$, and (c) a stagnation flame with a_p solved according to Eqs. ((22), (23)). Black arrows are direction of the gas velocity, blue arrows are direction of the particle velocity, gray lines represent the flame front and the dashed lines are the location of the stagnation plane. The particle colors indicate: gray an unburned particle, orange a partially oxidized particle, and red a fully oxidized particle. (For interpretation of the references to colour in this figure legend, the reader is referred to the web version of this article.)

Table 1
Simulation parameters.

Variable	Value	Unit
ρ_{Fe}	7.874	g/cm^3
ρ_{FeO_x}	5.745	g/cm^3
k_∞	75.0 $\times 10^7$	cm/s
T_a	14.4 $\times 10^3$	K
$c_{p,p}$	0.76	J/gK
Δh_c	4550	J/g

rate and solve for the corresponding mass fluxes, or the mass flux on the inlet is prescribed and the strain field is solved for. The latter is used in this work. Since only half of the domain is modeled, a mirror boundary condition is used at $x = 0$ for all properties of the gas phase. The tangential pressure gradient J is constant throughout the flow field, and an eigenvalue of the system. As it is expected that only a small fraction of particles cross the stagnation plane, no mirror boundary condition for the particles is used, instead they are removed when they cross x = 0.

3. Results

The in the previous section derived particle flow strain model is derived for a single particle. By tracking multiple particles in the Euler–Lagrange framework it is not restricted to mono-dispersed powders, i.e., Eq. (1) to Eq. (4) and Eqs. (22), (23) are solved on a per particle size bases. Nevertheless, as a first step, we will analyze mono-dispersed powders. In this section, the influence of particle strain, described by Eq. (22), on the flame structures is investigated. The influence of particles and the combination of particles and strain on thermo-diffusivity and preferential diffusion are not yet well understood. For that purpose, three cases are employed (1) a free unstrained flame where $a_p = a_g = 0$ and without slip ($u_p = u_g$), (2) an opposed twin flame where $a_p = a_g$ and (3) an opposed twin flame where the particle strain is solved according to Eqs. ((22), (23)), a schematic representation of these cases is shown in Fig. 2. For the particles, the parameters from Table 1 are used.

3.1. Preferential diffusion effects in a dispersed free flame

The freely propagating flame configuration as in [5,7], is a strain-free flame. When the flow is not strained ($a_p = a_g = 0$) and preferential diffusion ($\mathrm{Le}_i = 1$) effects are not at play in a gaseous flame, enthalpy and element mass fraction are constant through the flame [24]. However, in Fig. 3(a) it can be seen that the enthalpy and the fuel equivalence ratio $\phi = \frac{Z_{Fe}}{Z_O} \cdot s$, with Z_{Fe} and Z_O the element fraction of iron and oxygen in both solid and gas phase, and s the stoichiometric ratio assuming FeO as final product, are not constant through the flame for a mono-dispersed flame where the gaseous species have unity Lewis numbers. This can be explained by the fact that iron in the particles cannot diffuse, meaning $D_{Fe,m} = 0$, resulting in $\mathrm{Le}_{Fe} = \infty$. Also in the work of Wright et al. [25] it is mentioned that the mass diffusivity of the particles is practically absent and therefore an infinite Lewis number for the dispersed phase is to be expected. This indicates that preferential diffusion effects will always be present, when dealing with non-volatile dispersed phase combustion, at least when particle sizes are sufficiently large, such that Brownian motion can be neglected. For these simulations the diffusion coefficient obtained via the Stokes Einstein relation [26] is of order 10^{-12} m^2/s, which is much smaller than the diffusion coefficient of oxygen, being of order 10^{-5} m^2/s. Therefore, the diffusion due to Brownian motion can be neglected. The enthalpy and ϕ for a constant, non-unity Lewis number and mixture averaged diffusion coefficient are also shown in Fig. 3(a). Only small deviations are present compared to the ($\mathrm{Le}_i = 1$) case, because the Lewis number of oxygen is close to unity and the only gas phase species with Le_i. In the remainder of this work a mixture averaged diffusion coefficient for O_2 is used, which in this case is the same as the binary diffusion coefficient as only two species are present in the gas phase [27]. Fig. 3(b) shows the burned fraction $Y_b = 1 - \frac{m_{p,u}}{m_p}$ of the particles and the normalized oxygen fraction $Y^*_{O_2} = Y_{O_2}/Y_{O_2,0}$. As already observed in the work of Hazenberg and van Oijen [5], oxygen diffuses to the reaction front such that the normalized oxygen fraction starts to decrease before the particle burned fraction starts to decrease. This explains the local increase in ϕ and may result in local fuel-rich conditions even when inlet conditions are lean.

3.2. Flame structures

In this subsection, flame structures are compared of the three cases depicted in Fig. 2. For the particles, the parameters from Table 1 are used. A mono-dispersed powder with initial size $d_{p,0} = 10$ μm is utilized. The fuel equivalence ratio at the inlet is set to $\phi = 0.6$. The mass flux of gas at the inlet for cases (2) and (3) is $\dot{m}_g = 0.04$ g/cm^{2}s. For the free flame, case (1), there is no initial mass flux prescribed as for this case the mass flux at the inlet is an eigenvalue problem [23]. The x-axis values in all graphs in this section are not the actual position of

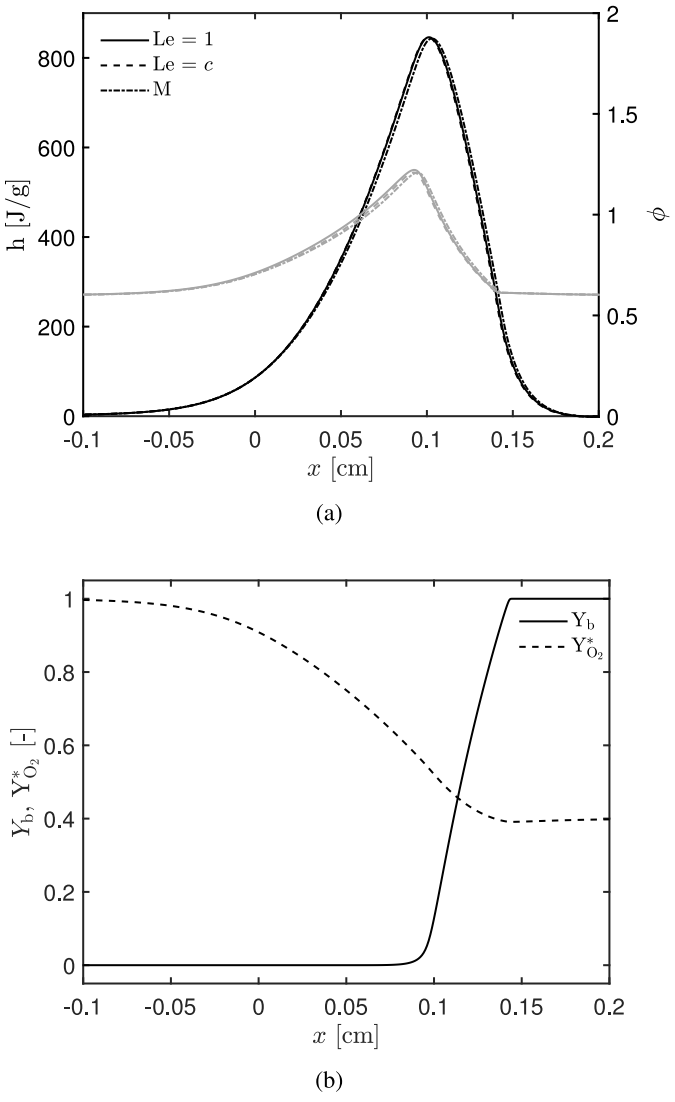

Fig. 3. (a) Profile of enthalpy (black) and ϕ (gray) through a one-dimensional lean (ϕ = 0.6) iron-dust/air flame without flame strain and unity Lewis numbers (solid), constant non-unity Lewis numbers (dashed) and mixture averaged diffusion coefficient (dash-dotted). (b) Profile of Y_b (solid) and $Y^*_{O_2}$ (dashed) at ϕ = 0.6 and Le = 1.

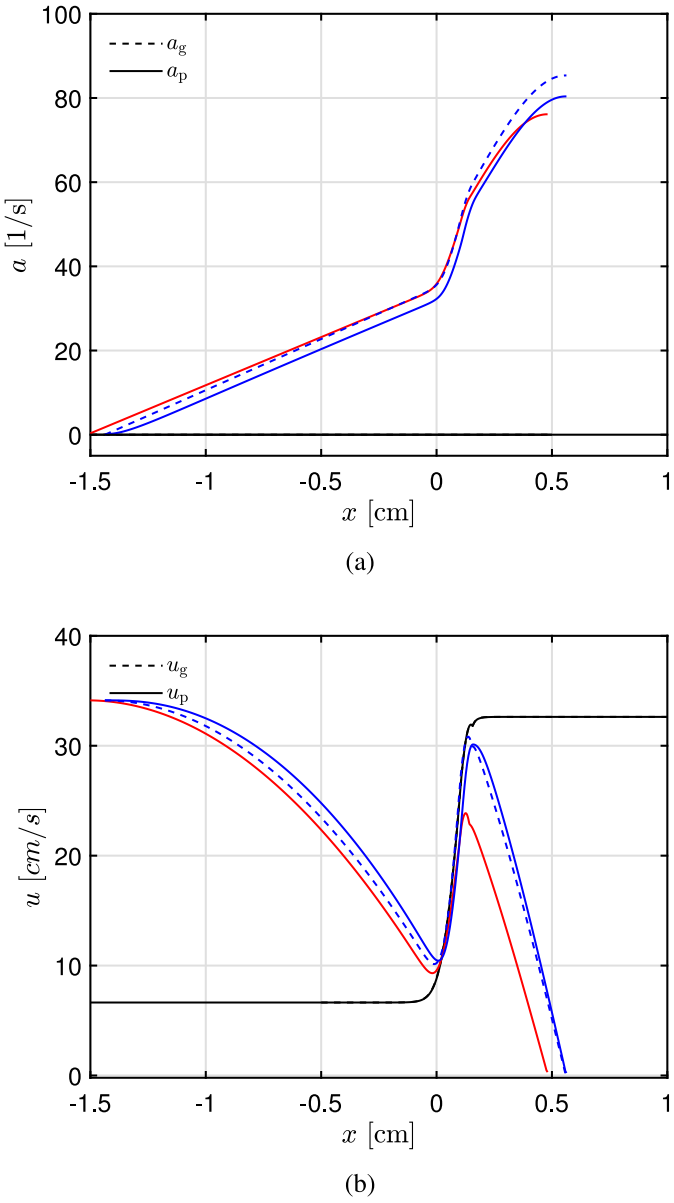

Fig. 4. (1) Free flame (black), (2) $a_p = a_g$ (red) and (3) resolved a_p (blue). (a) Profile of particle (solid) and gas (dashed) flow strain. (b) Velocity profile of gas (dashed) and particle (solid). Case (2) and (3) at ϕ = 0.6 and $\dot{m}$ = 0.04 g/cm^{2}s. (For interpretation of the references to colour in this figure legend, the reader is referred to the web version of this article.)

the counter-flow flames. Instead, the counter-flow flames are shifted in position such that the location of the maximum temperature coincides with that of the free flame.

In Fig. 4, the gas and particle flow strain and velocity profile of all three cases are shown. The flow strain of the free flame (black) is equal to zero as this is a zero flow strain case. The strain profiles of the $a_p = a_g$ (red) and resolved a_p (blue) cases are deviating from each other, especially in terms of maximum strain rate. Both cases have an inlet $\dot{m}_g$ = 0.04 g/cm^{2}s, but since the particle flow and gas flow in the $a_p = a_g$ case basically move as one inertia, being different from the resolved a_p case where the gas flow accelerates the particle flow and the particle flow decelerate the gas flow, different strain rates are obtained throughout the domain.

Fig. 4(b) displays the particle and gas velocity, where it can be seen that slip effects are at play for case (3). For cases (1) and (2) slip effects are not present as $a_p = a_g$ and also $u_p = u_g$. For case (3) it is observed that initially, as gas and particles move through the domain, the gas decelerates a bit faster than the particles. As soon as the particles start to burn and temperature rises, see Fig. 5, the velocities will increase and the gas velocity will slightly exceed the velocity of the particles. After that, particle and gas velocity decrease again resulting in particles having a somewhat higher velocity than the gas. The effect of particles being pulled by the gas flow, not being able to keep up with the gas flow and therefore decelerating the gas flow is similar to the accelerating and decelerating effects as seen in Fig. 4(a).

In Fig. 5, profiles of fuel equivalence ratio, mass fraction, temperature and specific enthalpy are shown. The equivalence ratio of the free flame is constant across the flame ($\phi_u = \phi_b$) as can be seen in Fig. 5(a). There are however local deviations due to preferential diffusion. In the preheat-zone, before any oxygen is consumed, oxygen gas has a higher velocity, because of diffusion to the reaction layer, which results in a decrease of oxygen concentration, see Fig. 5(b). Due to the decrease in oxygen mass fraction, the fuel equivalence ratio increases. As soon as the particles start to consume oxygen, the fuel equivalence ratio decreases again. The fuel equivalence ratio profile of the $a_p = a_g$ case also shows this preferential diffusion effect, indicated

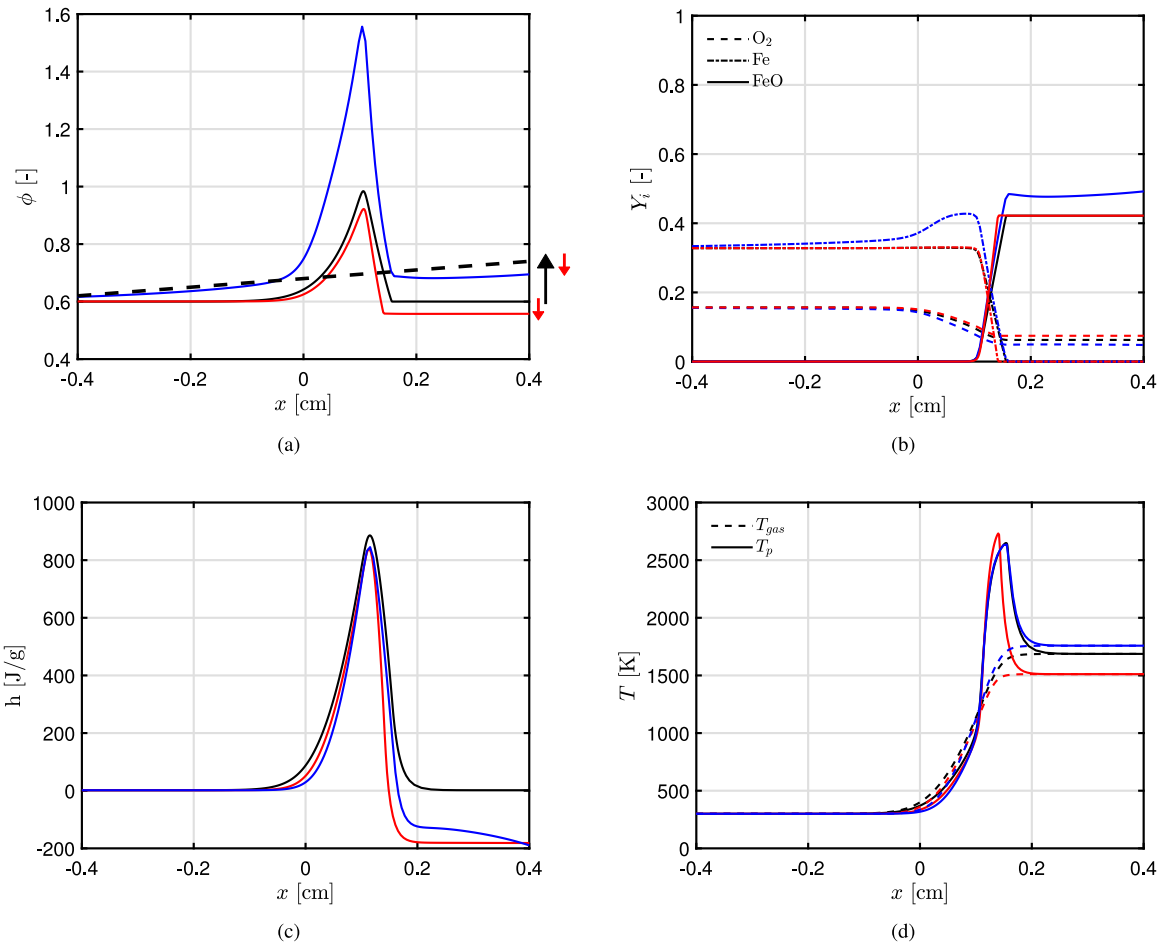

Fig. 5. (1) Free flame (black), (2) $a_p = a_g$ (red) and (3) resolved a_p (blue). (a) fuel equivalence ratio, where the dashed line is added for demonstrative purposes to show the influence of strain + inertia, which already plays a role on the unburned side. The black arrow indicates the influence of strain + inertia at the burned side and the red arrows represent the influence of strain + preferential diffusion at the burned side. (b) species mass fractions. (c) specific enthalpy profile. (d) temperature profile of particle (solid) and gas (dashed). Case (2) and (3) at $\phi = 0.6$ and $\dot{m} = 0.04$ g/cm^{2}s. (For interpretation of the references to colour in this figure legend, the reader is referred to the web version of this article.)

by the local increase in ϕ. This effect combined with flow straining results in relatively less straining of oxygen and therefore a decrease in fuel equivalence ratio at the burned side. The red arrows indicate the effect of strain and preferential diffusion. The fuel equivalence ratio of the resolved a_p case increases already before the preheat-zone, due to the combined effect of strain and inertia of the particles. This effect results in an enrichment of the fuel equivalence ratio as demonstrated by the black dashed line and the black arrow. On top of that there is the effect of strain and preferential diffusion, which has a decreasing influence on the fuel equivalence ratio. However, the inertia effect is dominant and therefore the fuel equivalence ratio at the burned side increases.

The specific enthalpy of the free flame is constant across the flame ($h_u = h_b$) as can be seen in Fig. 5(c). A peak in specific enthalpy occurs due to preferential diffusion. The $a_p = a_g$ case shows a similar peak due to preferential diffusion. There is a significant amount of leaking where the specific enthalpy is higher, see Fig. 4(a), such that a relative large amount of enthalpy is transported. Therefore, a lower specific enthalpy is observed at the burned side compared to the free flame. For case (3) we also observe a peak in specific enthalpy due to preferential diffusion and a decrease at the burned side due to the combined effect of strain and preferential diffusion. The latter effect seems lower than for case (2), due to the combined effect of strain and inertia. We also see that instead of reaching a plateau, which we do observe for case (1) and case (2), the specific enthalpy keeps decreasing. This is because the fuel equivalence ratio is still increasing due to faster leakage of the gas phase, indicating that near the stagnation plane the inertia effect will dominate.

The temperature profiles, shown in Fig. 5(d), of the three cases are not that different from each other until the maximum temperature is reached. Even though the specific enthalpy at the burned side has decreased, this does not mean that the flame temperature reduces, as can be seen in Fig. 5(d). One should keep in mind that the heat capacity of solid iron oxide is significantly lower, see Table 1, than the specific heat capacity of oxygen ($c_{p,O_2} > 1$ J/gK). Since the iron particles contribute to about half of the total mass at the end of the domain, see Fig. 5(b), the effective heat capacity of the mixture is severely lowered. Therefore, it is possible for the temperature to rise while the specific enthalpy decreases.

3.3. Particle flow strain for different particle sizes

In the previous section we have shown the importance of solving a separate model for the particle flow strain. In this section we will use that model to explore the influence of strain when using various particle sizes.

The absolute difference between gas and particle flow strain Δa for particle sizes of d_p = 4–20 μm with an interval of 1 μm are shown in Fig. 6(a). As the particle size increases, the particles are less capable of

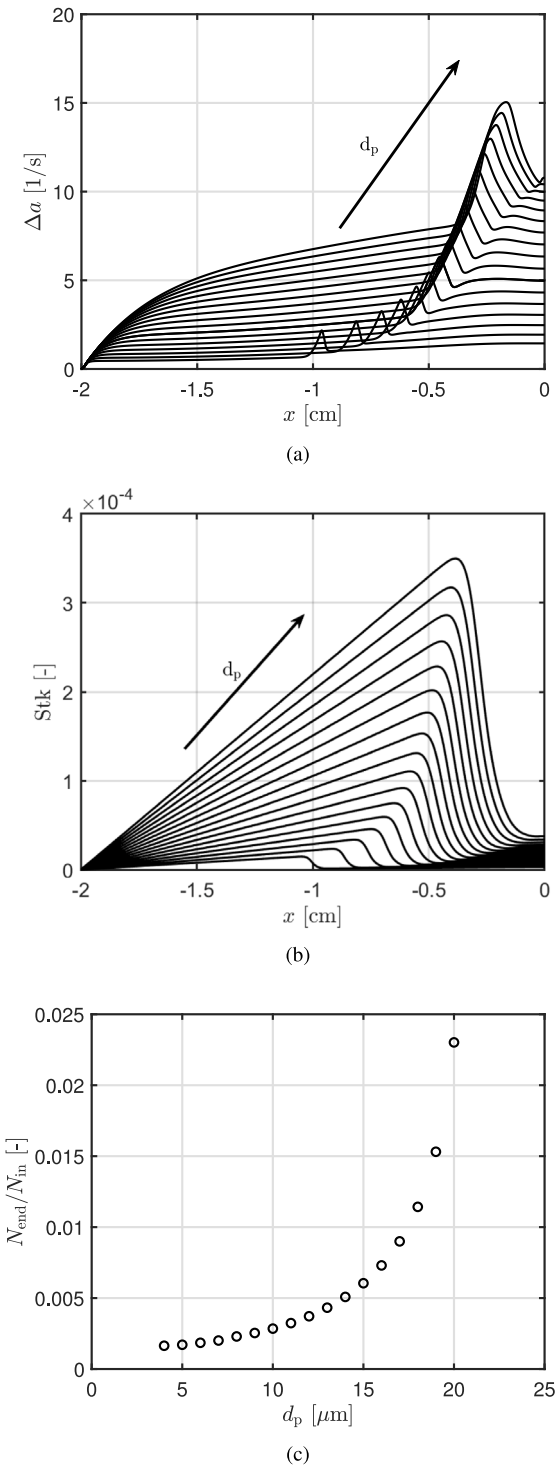

Fig. 6. (a) Absolute difference between gas flow strain and particle strain ($\Delta a = a_p - a_g$). (b) Stokes number profile. (c) Fraction of the number flux at outlet with respect to the inlet as function of particle size. Simulations are performed at $\phi = 0.6$ and $\dot{m} = 0.04$ g/cm^{2}s for particle sizes of d_p = 4:1:20 μm.

following the gas flow, indicated by the increase in the Stokes number (Stk = $\tau_p a_g$) for larger particles in Fig. 6(b). As a consequence, the combined effect of strain and inertia becomes more significant and the absolute difference in strain increases for larger particles. The increase in absolute strain difference results in an increase in both maximum

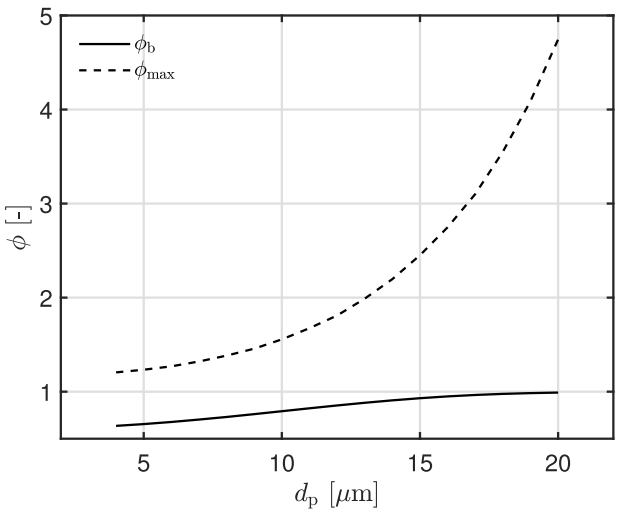

Fig. 7. Burned and maximum values of fuel equivalence ratio as function of particle size. Simulations are performed at $\phi = 0.6$ and $\dot{m} = 0.04$ g/cm^{2}s for particle sizes of d_p = 4:1:20 μm.

and burned ϕ, as can be seen in Fig. 7. This implies that, in counterflow experiments with a particle size distribution, the O_2 concentration encountered (and, hence, the local fuel-equivalence ratio) depends on this distribution.

In Fig. 6(c) the relative number flux at the outlet with respect to the inlet is presented to show only a relatively small amount of particles cross the stagnation plane. As particle size increases, the number of particles that cross the stagnation plane increases. As such, care should be taken when utilizing this model with large particles and high inlet mass fluxes.

3.4. Laminar flame speed prediction

There are several ways to perform flame speed predictions [11,28,29]. Here we numerically employ two variants of a similar method [11]. One key assumption for employing this method is that the flow is isothermal. Under this condition, a change in flow velocity in the y-direction is equal in magnitude to the change in velocity field in the x-direction with opposite sign, i.e. $\frac{dv}{dy} = -\frac{du}{dx}$ If the flow is not isothermal, one should correct for changes in gas density to obtain the true gas velocity. One of the options is the maximum heat release variant, where reference gas velocity and strain rate are used at the location of maximum heat release, Q_{max}, as the name of this variant already gives away. In Fig. 8 the heat release rate, strain rate, velocity profiles and the effect of strain on the gas velocity at the location of maximum heat release, $u_{g,ref}$, for $\phi_{in} = 0.6$ and mass flux $\dot{m}_g$ = 0.01–0.05 g/cm^{2}s are shown. The red dots in Fig. 8(a), indicate the position of Q_{max}, which is also the location where $u_{g,ref}$ and the corresponding strain rate are determined. The most accurate extrapolation to s_L is obtained when using the gas velocity, which is the reason why u_g is used instead of u_p. For an increased mass flux the maximum strain rate will increase and the particle inertia effects are more severe, see Figs. 8(b) and 8(c). Furthermore, the flame will move towards the stagnation point and at a high enough mass flux the flame will quench. Fig. 8(d) shows that $u_{g,ref}$ varies in a parabolic way with the strain rate. Hence, by parabolic extrapolating the values of $u_{g,ref}$ determined at the various strain rates, the intercept on the ordinate ($a_g = 0$), should give the laminar burning velocity s_L for the one-dimensional strain-free flame after correcting for gas expansion effects. This correction follows from conservation of mass for a flame with zero strain:

$$u_g^u \rho_g^u + u_p^u \rho_p^u = u_g^b \rho_g^b + u_p^b \rho_p^b, \tag{24}$$

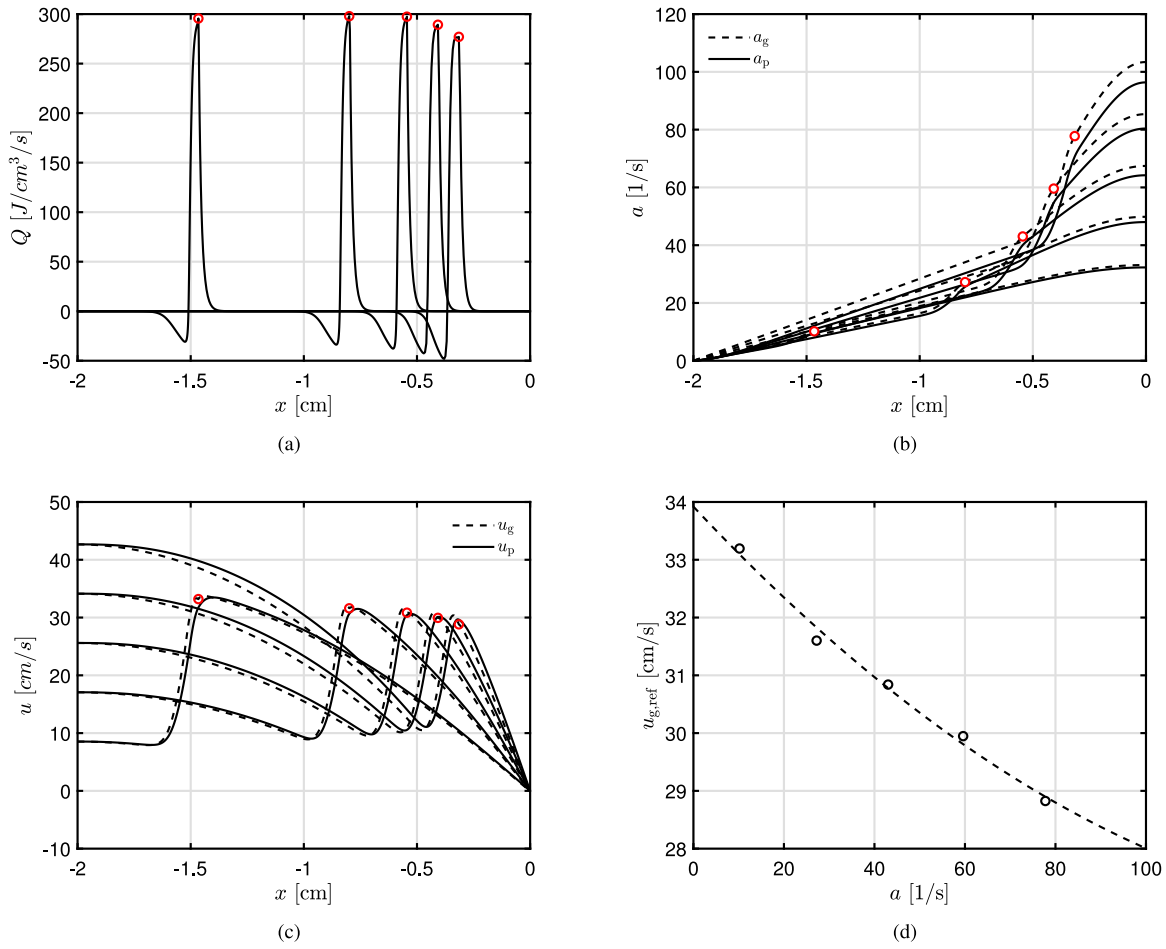

Fig. 8. s_L determination at the location of Q_{max}. (a) Heat release rate profiles. (b) Gas (dashed) and particle (solid) strain profiles. (c) Gas (dashed) and particle (solid) velocity profiles. (d) u_{ref} as function of strain rate. Simulations are performed at $\phi = 0.6$ and $\dot{m} = 0.0$–0.05 g/cm^{2}s, with an interval of 0.01 g/cm^{2}s, so each curve corresponds to a different mass flux. The red symbols indicate the location of Q_{max}. (For interpretation of the references to colour in this figure legend, the reader is referred to the web version of this article.)

$$s_L = \frac{\rho_g^b u_{g,ref}^b + u_p^b \rho_p^b - u_p^u \rho_p^u}{\rho_g^u}. \tag{25}$$

Here use is made of the fact that for a free flame the unburned gas velocity is equal to the laminar burning velocity, $u_g^u = s_L$, and that the velocity on the burned side is equal to the reference velocity $u_{g,ref}^b = u_g^b$. The maximum heat release is not something that can be measured very easily in practice, but a maximum light intensity can be measured instead. On top of that, in order to perform the gas expansion correction, the particle mass flux must be known very accurately, which is also still a challenge.

The other option to extrapolate to zero strain we will look into is the minimum velocity variant, where velocity and strain rate are measured at the location of minimum particle velocity, $u_{p,ref}$. For this variant we will use the particle velocity instead of the gas velocity, as this is what can actually be measured in experiments. In Fig. 9 the strain rate, velocity profiles and the effect of strain on the velocity at the location of minimum velocity for $\phi_{in} = 0.6$ and mass flux $\dot{m} = 0.0$–0.05 g/cm^2 are shown. Fig. 9(c) shows that $u_{p,ref}$ varies parabolic with the strain rate. Similar to Q_{max} method, we find that by parabolic extrapolating the values of $u_{p,ref}$ determined at the various strain rates, the intercept on the ordinate ($a = 0$), gives the laminar burning velocity s_L for the one-dimensional strain-free flame. In Fig. 9(c) the minimum gas velocity and its corresponding strain rate are also shown, where it can be seen that the dependency of the minimum velocity on the strain rate is different from that of the particles. Nevertheless, the laminar burning velocity determined with $u_{g,ref}$ is similar to the one determined with $u_{p,ref}$. In Fig. 9(d) the relative number flux at the symmetry plane with respect to the inlet is presented for several inlet mass fluxes to show that only a relatively small fraction of particles cross the stagnation plane. Initially, as the mass flux increases, the number of particles that cross the stagnation plane decreases. Thereafter, the number of particles that cross the stagnation plane increases linearly with increasing mass flux.

In Fig. 10 the Markstein lengths at the unburned side, $\mathcal{L}_u$ are shown for a range of fuel-equivalence ratios, which shows a roughly linear dependency. The Markstein length, is a measure of the response of the flame to strain [30], which relates the flame propagation rate s_L^* to the laminar (unstrained) flame speed s_L and the strain rate according to:

$$s_L^* = s_L - \mathcal{L}_u a. \tag{26}$$

Here, s_L^* is the burning velocity determined at the reference position and equal to $u_{g,ref}$ and s_L is the laminar burning velocity of a strain free flame (i.e., $u_{g,u}$ as in a free flame). The results of s_L predictions from the free flame and stagnation flame are presented and compared in Fig. 11. Overall, the flame speed predictions of both methods are good, but the Q_{max} method performs slightly better. Also, for $\phi_{in} > 0.8$ a larger discrepancy between the free flame s_L prediction and the u_{min} method stagnation flame predictions is observed. For these fuel equivalence ratios, fewer data points were available at very low strain rates, which probably influenced the extrapolation to zero strain rate.

Based on the two methods shown here, we would recommend to use the u_{min} method as this method is in good agreement with the free flame s_L prediction and more feasible from an experimental point of view.

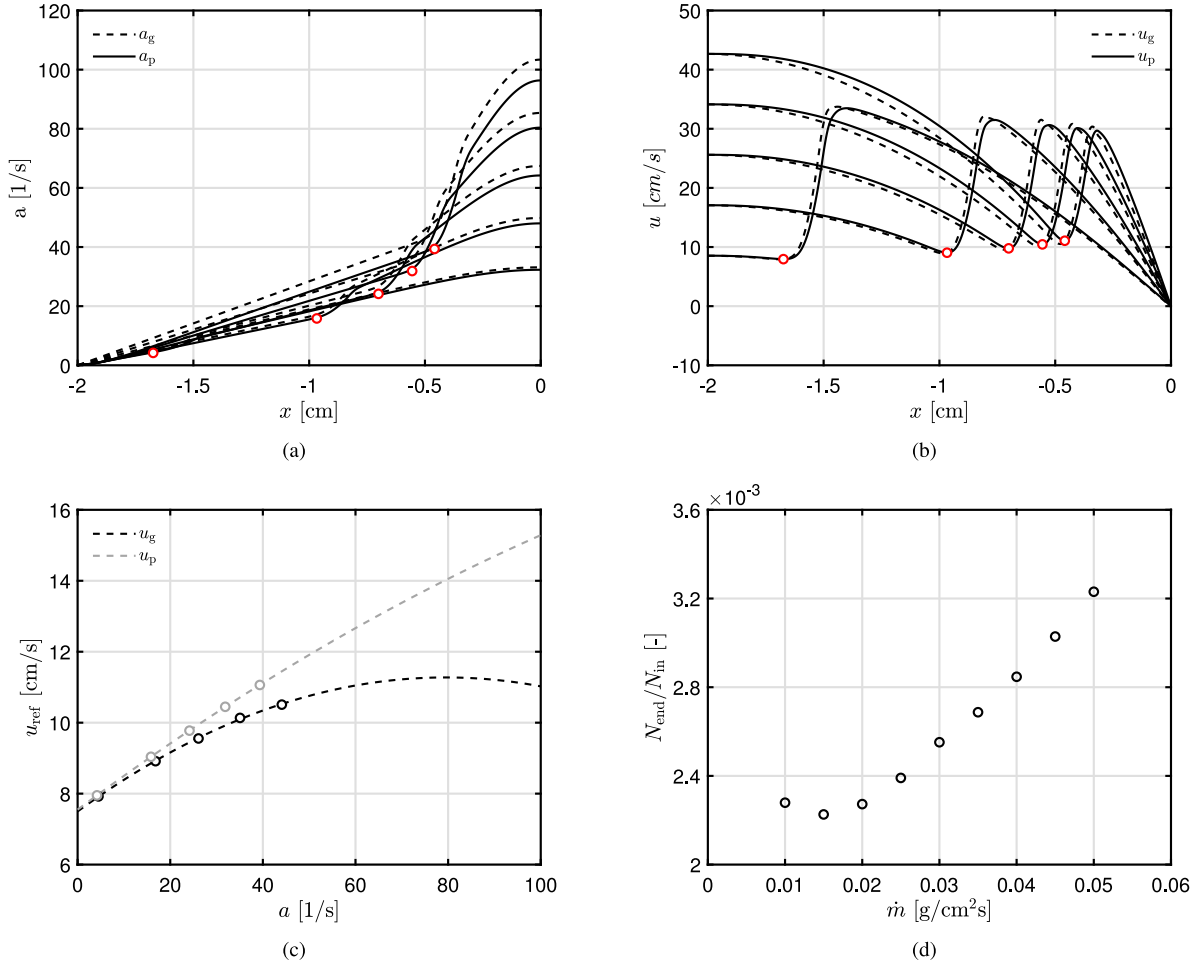

Fig. 9. s_L determination at the location of u_{min} method. (a) Gas (dashed) and particle (solid) strain profiles. (b) Gas (dashed) and particle (solid) velocity profiles. (c) u_{ref} as function of strain rate. (d) Fraction of the number flux at the symmetry plane with respect to the inlet as function of the mass flux. Simulations are performed at $\phi = 0.6$ and $\dot{m} = 0.0$–0.05 g/cm^{2}s, with an interval of 0.01 g/cm^{2}s. The red symbols indicate the location of u_{min}.

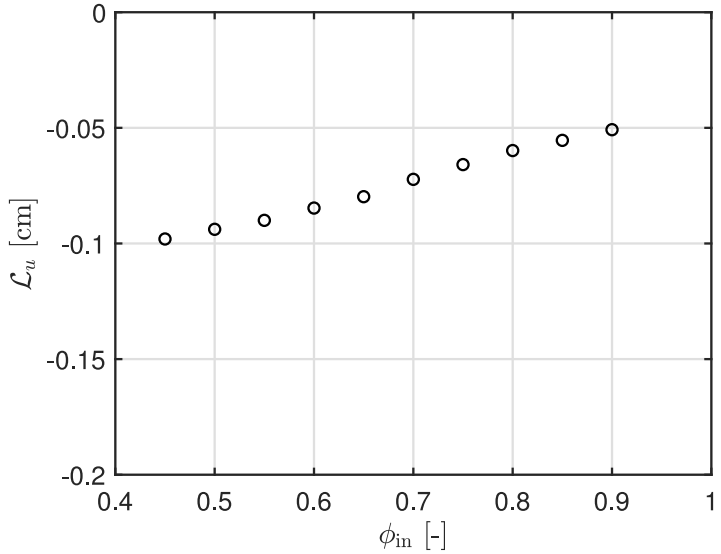

Fig. 10. Markstein length $\mathcal{L}$ for different fuel equivalence ratios.

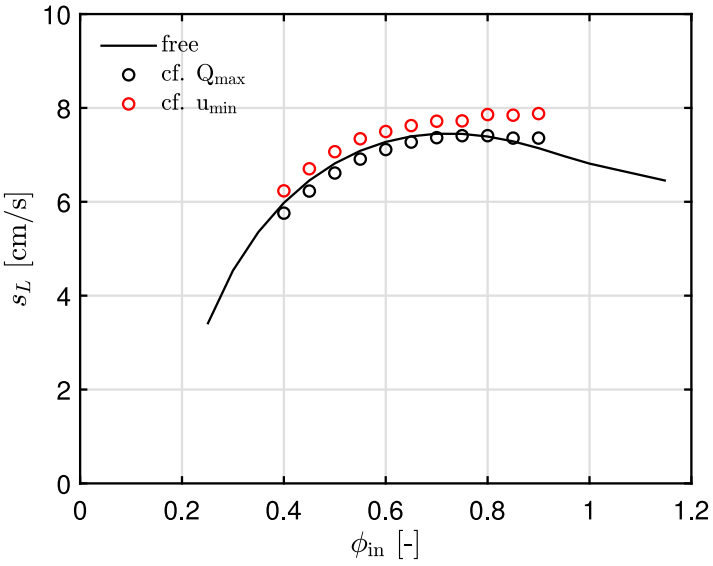

Fig. 11. Laminar flame speeds of 10 μm iron-dust-air mixtures (black solid) free flame, (black symbols) counter flow Q_{max} method, and (red symbols) counter flow u_{min} method. (For interpretation of the references to colour in this figure legend, the reader is referred to the web version of this article.)

4. Conclusions & discussion

In this work, a detailed 1D strain model is derived, assuming Re to be small. This detailed model is used to investigate the influence of strain on iron dust counter-flow flames. For now, the goal is to obtain more fundamental knowledge with the 1D model. Future steps include further validation of the 1D model against 2D and/or 3D simulation and to determine the limitations of the 1D model. An obvious limitation, are the higher order terms of the velocity, which are assumed zero in the 1D model. In gas phase flames, the magnitude of these higher order terms are small and are often neglected [8,12,15,16,28]. However, this assumption has to be validated for these dispersed flames.

Flame structures of a free flame, a counter-flow flame where gas flow strain equals particle flow strain and a counter-flow flame where the particle flow strain is resolved are compared to each other. Thereafter, the influence of strain on various particle sizes is briefly discussed. Lastly, a study is performed on the prediction of s_L using two variants of one method: the Q_{max} variant and the u_{min} variant.

First, it is concluded that preferential diffusion, due to the lack of diffusion in the fuel, is always at play in (iron) dust flames. This implies that the specific enthalpy and elemental fractions do not remain constant throughout the flame front. This is a relevant observation, as for positive strain the mixture becomes richer while the specific enthalpy decreases. However, this does not mean that the flame temperature reduces since the mixture c_p decreases.

The importance of solving a particle flow strain model instead of assuming particle flow having an equal strain as the gas flow is demonstrated: If the particle flow strain is assumed equal to the gas strain, the burned side of the flame actually becomes leaner instead of richer. The 'inertia effect' of the particles, which we showed dominant over preferential diffusion, is neglected when simply assuming the two strain rates to be equal to each other.

It is shown in the third subsection of the results that particle flow strain effects are of importance when performing experiments that are prone to strain. In these experiments each particle size experiences a different strain rate and thereby the PSD at the flame-front will be different than at the inlet. Future numerical studies could investigate this.

Finally, in the last subsection of the results a study is performed on the prediction of s_L with two different methods, the Q_{max} method and the u_{min}. Both methods are in good agreement with the free flame s_L prediction, but from an experimental point of view the u_{min} method is easier to use and therefore recommended. It is worth mentioning, that both options come with additional challenges when comparing to the prediction of s_L for gaseous flames. For instance, gravity forces acting on the particles will make it almost impossible to interpret data of counter-flow flames with a horizontal configuration. While in vertically oriented counter-flow flames, gravity will affect the top and bottom flame unsymmetrical.

CRediT authorship contribution statement

C.E.A.G van Gool: Conceptualization, Formal analysis, Investigation, Methodology, Software, Validation, Writing – original draft. **T. Hazenberg:** Conceptualization, Writing – review & editing. **J.A. van Oijen:** Conceptualization, Funding acquisition, Supervision, Writing – review & editing. **L.P.H. de Goey:** Conceptualization, Funding acquisition, Supervision, Writing – review & editing.

Declaration of competing interest

The authors declare that they have no known competing financial interests or personal relationships that could have appeared to influence the work reported in this paper.

Acknowledgments

This project has received funding from the European Research Council (ERC) under the European Union' Horizon 2020 research and innovation program under Grant Agreement no. 884916.

Appendix A

In Section 2.2, the transport equation for hydrodynamic strain a is introduced. Here, the derivation of Eq. (14) is demonstrated, which is slightly different from previous works [12,31] as it contains a source term accounting for the particle strain and here a slot instead of a jet configuration is assumed.

As mentioned in the main text, the counter-flow set-up in this work is assumed to be steady, flat and planar, such that all variables, i.e. ρ, T, Y_i, are only dependent on the x-coordinate, which is perpendicular to the flame surface. The only variable which depends on both the x- and y-coordinate, is the tangential velocity v. In Eq. (13), the definition for strain is given:

$$a(x) = \frac{\partial v}{\partial y}. \tag{A.1}$$

Integrating this equation with respect to y results in the following expression for the velocity,

$$v(x, y) = ay + C_1, \tag{A.2}$$

with C_1 as the integration constant. This integration constant must be equal to zero because there is no vertical velocity component at the center-line $y = 0$, such that the only solution for v is:

$$v(x, y) = ay. \tag{A.3}$$

The momentum conservation equation is defined as:

$$\frac{\partial \rho \boldsymbol{u}_g}{\partial t} + \nabla \cdot \left(\rho \boldsymbol{u}_g \boldsymbol{u}_g\right) = -\nabla p + \nabla \cdot \boldsymbol{\tau} + \rho_\mathrm{p} \boldsymbol{f} \tag{A.4}$$

where $\boldsymbol{u}_g$ is the flow velocity vector, p is the pressure, $\boldsymbol{\tau}$ is the viscous stress tensor and $\boldsymbol{f}$ denotes the external force vector representing the force between particles and gas. Bold face is used to indicate a vector.

When the strain expression and the continuity equation, Eq. (9) are substituted in the momentum equation (A.4) in x - direction, and taking the above assumptions (steady flow and variables only dependent on x) into consideration, one obtains [12,32]:

$$\rho u_\mathrm{g} \frac{\partial u_\mathrm{g}}{\partial x} = -\frac{\partial p}{\partial x} + \frac{\partial}{\partial x}\mu\left[\frac{4}{3}\frac{\partial u_\mathrm{g}}{\partial x} - \frac{2}{3}a_\mathrm{g}\right] + \mu\frac{\partial a_\mathrm{g}}{\partial x} + \rho_\mathrm{p} f_x, \tag{A.5}$$

where f_x is a body force between the particles and the gas, which has the form:

$$f_x = \frac{u_\mathrm{g} - u_\mathrm{p}}{\tau}, \tag{A.6}$$

where u_g and u_p are exclusively a function of x, such that f_x is also only a function of x.

Similarly, an expression can be obtained for the momentum equation in the y - direction:

$$\rho u_\mathrm{g} \frac{\partial v_\mathrm{g}}{\partial x} + \rho v_\mathrm{g} a_\mathrm{g} = -\frac{\partial p}{\partial y} + \frac{\partial}{\partial x}\mu\frac{\partial v_\mathrm{g}}{\partial x} + \frac{\partial}{\partial x}\mu\left[\frac{4}{3}a_\mathrm{g} - \frac{2}{3}\frac{\partial u_\mathrm{g}}{\partial x}\right] + \rho_\mathrm{p} f_y, \tag{A.7}$$

with f_y:

$$f_y = \frac{v_\mathrm{g} - v_\mathrm{p}}{\tau}, \tag{A.8}$$

where v and v_p being a function of both x and y.

Substituting Eq. (A.3) in Eq. (A.7) and dividing by y yields the following expressions for the momentum equations in x- and y- direction, where the pressure term is isolated:

$$\frac{\partial p}{\partial x} = -\rho u_\mathrm{g}\frac{\partial u_\mathrm{g}}{\partial x} + \frac{\partial}{\partial x}\mu\left[\frac{4}{3}\frac{\partial u_\mathrm{g}}{\partial x} - \frac{2}{3}a_\mathrm{g}\right] + \mu\frac{\partial a_\mathrm{g}}{\partial x} + \rho_\mathrm{p} f_x, \tag{A.9}$$

$$\frac{1}{y}\frac{\partial p}{\partial y} = -\rho u_\mathrm{g}\frac{\partial a_\mathrm{g}}{\partial x} - \rho a_\mathrm{g}^2 + \frac{\partial}{\partial x}\mu\frac{\partial a_\mathrm{g}}{\partial x} + \rho_\mathrm{p} f_y. \tag{A.10}$$

Taking the derivative of Eq. (A.9) with respect to y, and subsequent division by y, results in the following expression:

$$\frac{1}{y}\frac{\partial}{\partial y}\left(\frac{\partial p}{\partial x}\right) = \frac{1}{y}\frac{\partial}{\partial x}\left(\frac{\partial p}{\partial y}\right) = \frac{\partial}{\partial x}\left(\frac{1}{y}\frac{\partial p}{\partial y}\right) = 0, \tag{A.11}$$

indicating that the left hand side of Eq. (A.10) can only be a constant. This term is denoted by $-J$, which leads to the final transport equation for a.

$$\rho u_\mathrm{g}\frac{\partial a_\mathrm{g}}{\partial x} - \frac{\partial}{\partial x}\mu\frac{\partial a_\mathrm{g}}{\partial x} = \rho_\mathrm{p} f_y + J - \rho a_\mathrm{g}^2. \tag{A.12}$$

Using the momentum transfer between particles and gas, Eq. (A.8), and the linear approximation for the strain, Eq. (A.3), we obtain:

$$\frac{\partial\left(\rho u_\mathrm{g} a_\mathrm{g}\right)}{\partial x} - \frac{\partial}{\partial x}\left(\mu\frac{\partial a_\mathrm{g}}{\partial x}\right) = S_a + J - \rho a_\mathrm{g}^2 \tag{A.13}$$

Appendix B

The solution of Eq. (18), relies on the assumption that τ and a_g are constant and positive. Here we will show that numerically solving Eq. (18) with a non-constant a_g yields a similar solution for a_p as the solution obtained with the reduced model in Eq. (22). For this purpose, we consider a non-reactive particle subjected to various gas strain flow fields. Results for various shapes of the gas strain field are shown in Fig. B.12. In Fig. B.12(a) the gas flow strain rate (black dotted line) is a linear function that increases to 10 1/s in 1 s. The particle strain rate obtained by solving Eq. (22), which we will name the reduced model is in very good agreement with the particle strain rate obtained by solving Eq. (18), to which we will refer as detailed model. Both models have a slight delay compared to the gas flow strain rate, due to the inertia of the particles. In Fig. B.12(b) the gas flow strain rate is again a linear function, but now it increases to 100 1/s in 1 s. Again, we see that the detailed and reduced model predict the same behavior.

The next gas flow strain profile we will look at is that of a pulse, shown in Figs. B.12(c), B.12(d), where the first is a pulse with amplitude 10 1/s and the latter a pulse with amplitude 100 1/s. Again, the particle flow strain lags the gas flow strain. For the pulse with an amplitude of 10 1/s there is hardly any difference visible between the detailed and reduced model. A slight difference between the two models is visible for the pulse with an amplitude 100 1/s. However, this difference is still very small.

Lastly, the particle is subjected to a sinusoidal gas flow strain profile displayed in Figs. B.12(e), B.12(f), where the first sine function has amplitude 10 1/s and the latter has amplitude 100 1/s. A lag between the gas flow strain and the particle flow is clearly visible in both figures. For both amplitudes, the particle flow strain rate of the detailed and reduced model are practically laying on top of each other.

Based on these results, we conclude that the reduced strain model, Eq. (22), does not introduce significant errors.

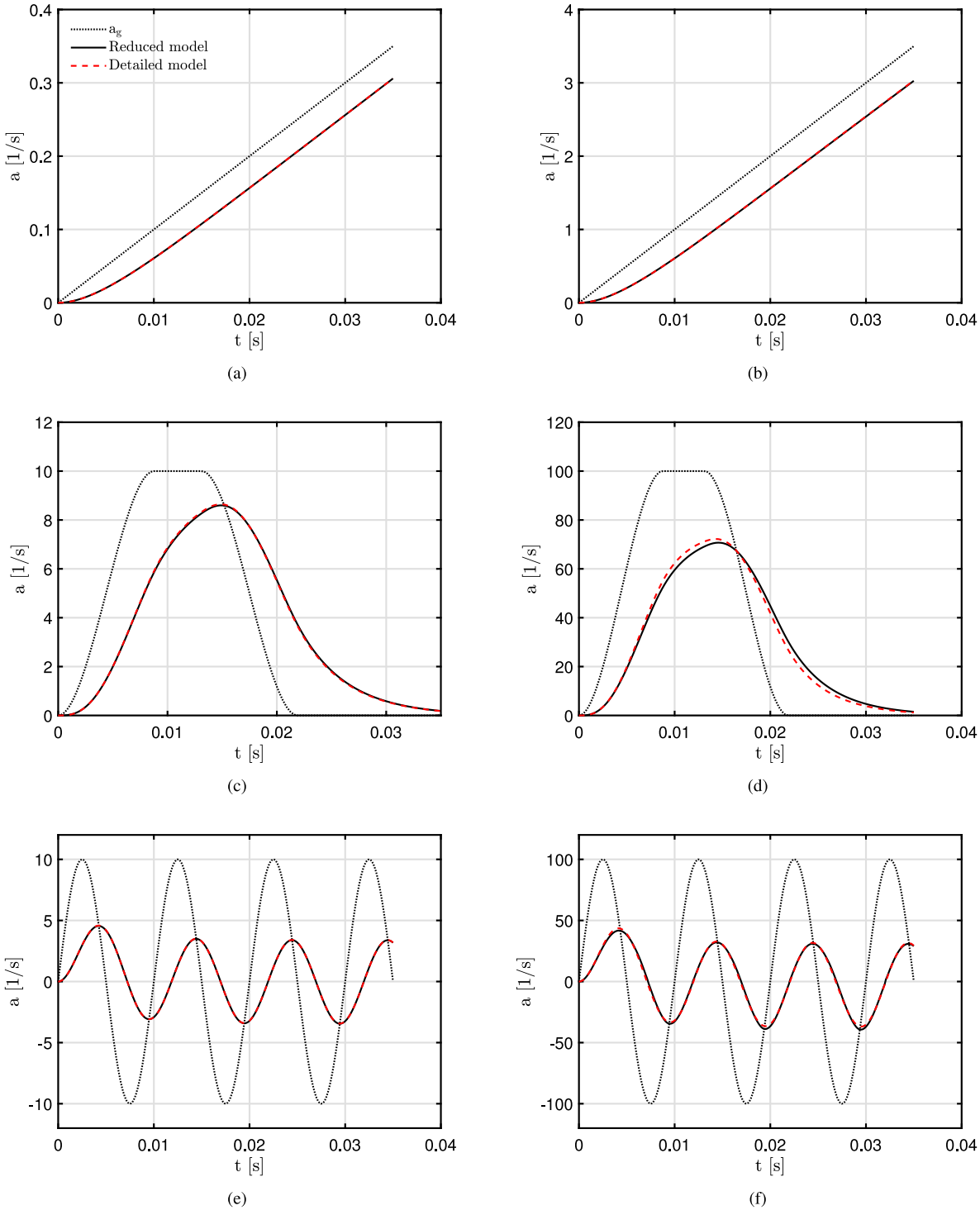

Fig. B.12. Gas flow strain rate (black dotted), particle flow strain rate with reduced model (black solid), particle flow strain rate with reduced model (red dashed). Gas flow strain is: (a) a linear function to 10 1/s in 1 s. (b) a linear function to 100 1/s in 1 s. (c) a pulse with amplitude 10 1/s. (d) a pulse with amplitude 100, (e) a sine with amplitude 10 and f = 100 Hz, (f) a sine with amplitude 100 and f = 100 Hz. (For interpretation of the references to colour in this figure legend, the reader is referred to the web version of this article.)

References

[1] D. Mignard, C. Pritchard, A review of the sponge iron process for the storage and transmission of remotely generated marine energy, Int. J. Hydrog. Energy 32 (18) (2007) 5039–5049.

[2] J.M. Bergthorson, S. Goroshin, M.J. Soo, P. Julien, J. Palecka, D.L. Frost, D.J. Jarvis, Direct combustion of recyclable metal fuels for zero-carbon heat and power, Appl. Energy 160 (2015) 368–382.

[3] J. Sun, R. Dobashi, T. Hirano, Structure of flames propagating through metal particle clouds and behavior of particles, Proc. Combust. Inst. 27 (2) (1998) 2405–2411.

[4] F.D. Tang, S. Goroshin, A. Higgins, J.H.S. Lee, Flame propagation and quenching in iron dust clouds, Proc. Combust. Inst. 32 (2) (2009) 1905–1912.

[5] T. Hazenberg, J.A. Van Oijen, Structures and burning velocities of flames in iron aerosols, Proc. Combust. Inst. 38 (3) (2021) 4383–4390.

[6] A. Ravi, L.P.H. de Goey, J.A. Van Oijen, Flame structure and burning velocity of flames propagating in binary iron aerosols, Proc. Combust. Inst. 39 (2022).

[7] C.E.A.G. van Gool, L.C. Thijs, W.J.S. Ramaekers, J.A. van Oijen, L.P.H. de Goey, Particle equilibrium composition model for iron dust combustion, Appl. Energy Combust. Sci. 13 (2023) 100115.

[8] B. Karlovitz, D. Denniston, D. Knapschaefer, F. Wells, Studies on turbulent flames: A. flame propagation across velocity gradients b. turbulence measurement in flames, in: Symposium (International) on Combustion, vol. 4, (no. 1) 1953, pp. 613–620.

[9] B. Lewis, G. von Elbe, Combustion, Flames and Explosions of Gases, Academic Press, New York, 1961.

[10] G.H. Markstein, Nonsteady Flame Propagation, Pergamon Press, Oxford, 1964.

[11] C.K. Wu, C.K. Law, On the determination of laminar flame speeds from stretched flames, in: Symposium (International) on Combustion, vol. 20, (no. 1) 1985, pp. 1941–1949.

[12] G. Dixon-Lewis, Structure of laminar flames, in: Symposium (International) on Combustion, vol. 23, (no. 1) 1991, pp. 305–324.

[13] L.P.H.D. Goey, J.H.M.T.T. Boonkkamp, A mass-based definition of flame stretch for flames with finite thickness, Combust. Sci. Technol. 122 (1–6) (1997) 399–405, http://dx.doi.org/10.1080/00102209708935618.

[14] J.A. van Oijen, A. Donini, R.J.M. Bastiaans, J.H.M. ten Thije Boonkkamp, L.P.H. de Goey, State-of-the-art in premixed combustion modeling using flamelet generated manifolds, Prog. Energy Combust. Sci. 57 (2016) 30–74.

[15] G. Continillo, W.A. Sirignano, Counterflow spray combustion modeling, Combust. Flame 81 (3) (1990) 325–340.

[16] D. Graves, J.O.L. Wendt, Flammability characteristics and structure of a pulverized coal, laminar opposed jet diffusion flame, in: Symposium (International) on Combustion, vol. 19, (no. 1) 1982, pp. 1189–1196.

[17] X. Wen, A. Scholtissek, J. van Oijen, J. Bergthorson, C. Hasse, Numerical modeling of pulverized iron flames in a multidimensional hot counterflow burner, Combust. Flame 248 (2023) 112572.

[18] J. Zhang, Z. Xia, L. Ma, O. Stein, Y. Feng, T.D. Luu, A. Kronenburg, Sensitivity of flame structure and flame speed in numerical simulations of laminar aluminum dust counterflow flames, Combust. Flame 245 (2022) 112363.

[19] R. Clift, J.R. Grace, M.E. Weber, Bubbles, Drops, and Particles, Courier Corporation, 2005.

[20] F.L. Sacomano Filho, N. Speelman, J.A. van Oijen, L.P.H. de Goey, A. Sadiki, J. Janicka, Numerical analyses of laminar flames propagating in droplet mists using detailed and tabulated chemistry, Combust. Theory Model. 22 (5) (2018) 998–1032.

[21] T. Hazenberg, An Eulerian-Lagrangian Approach for Simulating Heterogeneous Combustion of Metal Fuels (Master's thesis), University of Technology Eindhoven, Eindhoven, The Netherlands, 2019.

[22] C.K. Law, Combustion Physics, Cambridge University Press, 2006.

[23] L.M.T. Somers, The Simulation of Flat Flames with Detailed and Reduced Chemical Models (Master's thesis), University of Technology Eindhoven, Eindhoven, The Netherlands, 1994.

[24] J.A.M. de Swart, Modeling and Analysis of Flame Stretch and Preferential Diffusion in Premixed Flames, Mechanical Engineering, (Ph.D. thesis), 2009.

[25] A. Wright, A.J. Higgins, S. Goroshin, The discrete regime of flame propagation in metal particulate clouds, Combust. Sci. Technol. 188 (11–12) (2016) 2178–2199.

[26] C.C. Miller, J. Walker, The stokes-einstein law for diffusion in solution, Proc. R. Soc. London. Series A Contain. Pap. Math. Phys. Character 106 (740) (1924) 724–749.

[27] R.K. Ross Taylor, Multicomponent Mass Transfer, Har/Dis Edition, in: Wiley series in chemical engineering, Wiley, 1993.

[28] C. Law, Dynamics of stretched flames, in: Symposium (International) on Combustion, vol. 22, (no. 1) 1989, pp. 1381–1402.

[29] J. Tien, M. Matalon, On the burning velocity of stretched flames, Combust. Flame 84 (3) (1991) 238–248.

[30] L.-K. Tseng, M. Ismail, G. Faeth, Laminar burning velocities and Markstein numbers of hydrocarbonair flames, Combust. Flame 95 (4) (1993) 410–426.

[31] W. Ramaekers, Development of flamelet generated manifolds for partially-premixed flame simulations, phd thesis 1 (research tu/e / graduation tu/e), Mech. Eng. (2011).

[32] G. Stahl, J. Warnatz, Numerical investigation of time-dependent properties and extinction of strained methane and propane-air flamelets, Combust. Flame 85 (3) (1991) 285–299.